

INFORMATION TO USERS

This manuscript has been reproduced from the microfilm master. UMI films the text directly from the original or copy submitted. Thus, some thesis and dissertation copies are in typewriter face, while others may be from any type of computer printer.

The quality of this reproduction is dependent upon the quality of the copy submitted. Broken or indistinct print, colored or poor quality illustrations and photographs, print bleedthrough, substandard margins, and improper alignment can adversely affect reproduction.

In the unlikely event that the author did not send UMI a complete manuscript and there are missing pages, these will be noted. Also, if unauthorized copyright material had to be removed, a note will indicate the deletion.

Oversize materials (e.g., maps, drawings, charts) are reproduced by sectioning the original, beginning at the upper left-hand corner and continuing from left to right in equal sections with small overlaps. Each original is also photographed in one exposure and is included in reduced form at the back of the book.

Photographs included in the original manuscript have been reproduced xerographically in this copy. Higher quality 6" x 9" black and white photographic prints are available for any photographs or illustrations appearing in this copy for an additional charge. Contact UMI directly to order.



University Microfilms International
A Bell & Howell Information Company
300 North Zeeb Road, Ann Arbor, MI 48106-1346 USA
313/761-4700 800/521-0600

Order Number 1345372

**Re-calibration of IRAS flux measurements at 25, 60 and 100 μ m
using stellar atmosphere models**

Kirby, Diana Jill, M.S.

The University of Arizona, 1991

U·M·I

**300 N. Zeeb Rd.
Ann Arbor, MI 48106**

RE-CALIBRATION OF IRAS FLUX MEASUREMENTS
AT 25, 60 AND 100 μ m
USING STELLAR ATMOSPHERE MODELS

by
Diana Jill Kirby

A Thesis Submitted to the Faculty of the
DEPARTMENT OF ASTRONOMY
In Partial Fulfillment of the Requirements
For the Degree of
MASTER OF SCIENCE
In the Graduate College
THE UNIVERSITY OF ARIZONA

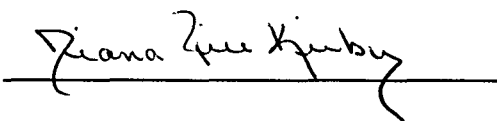
1 9 9 1

STATEMENT BY AUTHOR

This thesis has been submitted in partial fulfillment of requirements for an advanced degree at The University of Arizona and is deposited in the University Library to be made available to borrowers under rules of the Library.

Brief quotations from this thesis are allowable without special permission, provided that accurate acknowledge of source is made. Requests for permission for extended quotation or reproduction of this manuscript in whole or in part may be granted by the head of the major department or the Dean of the Graduate College when in his or her judgement the proposed use of the material is in the interests of scholarship. In all other instances, however, permission must be obtained from the author.

SIGNED



APPROVAL BY THESIS DIRECTOR

This thesis has been approved on the date shown below:



George H. Rieke
Professor of Astronomy

6/21/1991
Date

TABLE OF CONTENTS

LIST OF TABLES	4
ABSTRACT	5
I. INTRODUCTION	6
a. Filters	6
b. Evidence for a Leak	10
c. Calibration Techniques	11
d. IRAS Calibrations	12
II. FOURIER ANALYSIS OF THE IRAS BEAM PROFILES	15
a. Introduction	15
b. Beam Profile Analysis	16
c. Power Spectrum Analysis	17
d. Estimation of Leak	24
e. Conclusions	26
III. CALIBRATIONS	28
a. Introduction	28
b. Background	28
c. Re-calibrations	29
d. Conclusions	34
IV. CONCLUSIONS	36
APPENDIX A: TABLES	38
APPENDIX B: FIGURES	51
REFERENCES	61

LIST OF TABLES

Table 1	Status of Calibrations Stars
Table 2	Comparison of Colors Derived from New Stellar Atmosphere Models
Table 3	Predicted and Measured Fluxes
Table 4	25 μ m Magnitudes and Colors
Table 5	60 μ m Magnitudes and Colors
Table 6	100 μ m Magnitudes and Colors
Table 7	Summary of Calibration Corrections

ABSTRACT

Beam profiles from the Infrared Astronomical Satellite (IRAS) at 60 and 100 μ m and for both hot and cold sources are analyzed using Fourier techniques to check the efficiency of the short wavelength blockage in the 60 and 100 μ m filters. Comparison of these power spectra with the expected passbands and an estimate of the noise supports the hypothesis that the 100 μ m filters have a short wavelength leak of $14.3 \pm 3.6\%$, but there is no detectable leak in the 60 μ m filters. Following decrement of the 100 μ m flux by 14.3%, stellar atmosphere models are anchored at 12 μ m to the IRAS flux measurements for 33 chosen stars and predicted flux measurements at 25, 60 and 100 μ m are computed. Comparison of these predictions with those measured by IRAS shows that the IRAS measurements are overestimated at 25 and 60 μ m and underestimated at 100 μ m with regard to atmospheric models.

I. INTRODUCTION

In November 1983, the Infrared Astronomical Satellite (IRAS) completed a survey of 96% of the sky at effective wavelengths of 12, 25, 60 and 100 μ m. Since that time, some questions have arisen concerning the effectiveness of the filters on the 60 and 100 μ m detectors in blocking shorter wavelengths. Additionally, new stellar atmosphere models are now available which permit the calibration of the three longer wavelengths directly from the 12 μ m calibrations. The purpose of this research is to investigate the effectiveness of the 60 and 100 μ m filters by looking for evidence of spectral frequencies outside the pass bands of the detectors in question using Fourier techniques. Once the question of the short wavelength blocking in the long wavelength detectors is resolved, new stellar atmosphere models will be used to derive a calibration for the 25, 60 and 100 μ m wavelengths directly from the 12 μ m calibration. This calibration will be compared to the original IRAS calibration and a correction factor for each band will be computed.

a. Make-up of the 60 and 100 μ m filters.

Out-of-band rejection in the long wavelength detectors is dependent on the characteristics of the Ge:Ga detectors and the configuration of blocking filters along with a multi-layer interference film (MLIF) on each filter. A diagram of these

filters and summary of characteristics is found on pages II-15,16 of the IRAS Explanatory Supplement (Beichman et al., 1984).

The specific list of filter material is as follows:

	60 μ m	100 μ m
Sapphire:	1mm	1mm
ZnO :	14 μ m	-
KRS-5:	.75mm	-
Diamond Powder:	-	15 μ m
CaF ₂ :	-	1mm
Polyethylene	-	28 μ m
KCl:	-	1mm
Parylene-C	2 μ m	2 μ m
Germanium	50 layers	50 layers

These combinations of substances should allow radiation to pass only between 27 and 87 μ m for the 60 μ m detectors and 65 and 120 μ m for the 100 μ m detectors.

For the 60 μ m detectors, the long wavelength cutoff and blocking are provided by the KRS-5. The short wavelength cuton is set by the sapphire and the MLIF. Short wavelength blocking is the result of a combination of the MLIF, the sapphire and the ZnO powder (Supplement, II-16). The germanium is applied to both sides of the sapphire in order to block radiation shortward of 1 μ m.

For the 100 μ m detectors, the long wavelength cutoff and blocking are the result of the Ge:Ga detectors (Supplement II-16). The short wavelength cuton is set by the KCl and the short wavelength blocking comes from the combination of

substances listed above. The diamond powder preferentially scatters short wavelength radiation out of the beam path and the germanium blocks the very short wavelength radiation.

These filters are thought to be very effective between $7\mu\text{m}$ and their respective short wavelength cutons and shortward of $1.6\mu\text{m}$. Any leaks will occur between 1.6 and $7\mu\text{m}$. This will give the filters a bimodal response; two peaks will appear in the spectral energy distribution, one of which will lie within the expected passband and one of which will be between 1.6 and $7\mu\text{m}$. Under Fourier analysis, evidence for unwanted radiation between 1.6 and $7\mu\text{m}$ will show up at the higher spatial frequencies and so can be distinguished from other effects which manifest themselves only at lower spatial frequencies.

Figure 1 shows what is known about the spectral characteristics of a short wavelength leak in the $100\mu\text{m}$ filters. The solid curve is the expected transmission of the crystal filter elements and the field lens (the Ge, KCl, CaF_2 , and sapphire). The dotted curve is the spectrum of a 4000°K blackbody which is similar to the spectral energy distribution of the cool stars used in infrared calibrations. The short-dash curve shows the expected spectral response for the detectors under elementary theory in which each photon produces identical response independent of its wavelength. The long-dashed line is the measurement of the leak in the Short Wavelength

Blocker (a dielectric stack on the sapphire element). These measurements are from the "End Item Data Package" provided with the filters by their supplier, Infrared Laboratories, Inc., dated 21 November 1978.

In addition to the elements shown in Figure 1, the filter stack included a layer of diamond powder deposited on the CaF_2 that scattered short wavelength radiation out of the beam. The dot-dash line in the figure is the product of all the other spectral dependencies and shows the net wavelength dependence of the leak in the absence of any spectral dependence for the scattering by diamond particles. The effective wavelength of the leak indicated by this line is $3.5\mu\text{m}$. The wavelength dependence of the transmission through the diamond particles is not known; if these particles had voids in their distribution that are large compared with the near infrared wavelengths of the leak, then the transmission would be roughly neutral and no correction in effective wavelength would be required. If the leak is predominantly scattered light that emerges into the beam incident onto the detectors, then the leak would be strongly biased toward the longer wavelengths of the passband permitted by the crystals; scaling from measurements of the cuton behavior of similar filters, the effective wavelength could be as long as $4.5\mu\text{m}$ (Armstrong and Low, 1974).

It is also important to note that the filter manufacturer

did measure the net leak of four 100 μ m detectors in the 1.3 to 8 μ m band and found them to be identical to within \pm 20% (End Item Data Package, op.cit.). It is therefore reasonable to assume that if one of the 100 μ m detectors leaks, the others will have a similar response.

b. Evidence of a Short Wavelength Leak.

There is evidence both for and against the existence of short wavelength leaks in the 60 and 100 μ m detector filters. Pre-launch tests indicated leaks of 2% ($T = 2,000^{\circ}$ K) and 8% ($T = 10,000^{\circ}$ K) through the 60 μ m filters (Supplement, II-17). The response of the 100 μ m detectors was assumed to be similar although the material came from different sources. The 100 μ m detectors were not tested.

Comparison of IRAS measurements of Uranus and Neptune with measurements made in the Kuiper Airborne Observatory (KAO) also lends weight to the possibility of a leak at short wavelengths. IRAS in-flight measurements of Uranus ($T = 60^{\circ}$ K) were low (by 20% at 60 μ m) when compared to measurements made by Hildebrand et. al. (1984) in the KAO (Supplement, VI-28-30). This discrepancy could be explained by a leak of 20% or larger in the 60 μ m detector channels at the effective temperatures of the stars used as calibrators since the hotter stellar flux would have been overestimated.

The Supplement (VI-27,29) cites good fit to both asteroid and stellar models and near constant stellar colors with

effective temperature as the strongest evidence against the existence of a short wavelength leak.

c. Calibration Techniques.

Calibration of wavelengths which cannot be measured directly from the ground or otherwise absolutely calibrated requires the extrapolation of shorter wavelength calibrations. This is commonly done using models of physically simple sources. The choice of initial calibration sources and models is critical in this process. Normally, stars are chosen as calibration sources for wavelengths running out to $60\mu\text{m}$ since they are thought to be well understood and therefore readily modelled. For calibrations past $60\mu\text{m}$, low signal-to-noise ratios and uncertain models have, in the past, precluded the use of stars. Calibrations past $60\mu\text{m}$ have been made using colder sources such as asteroids.

Asteroids are both more difficult to model and less thoroughly understood than stars so their use as calibration standards involves new levels of complexity. The energy emitted by asteroids is generated by the absorption of sunlight. Flux levels for individual asteroids will vary depending on current orbital distance from the sun. Flux levels may also vary widely depending upon viewing angle from the earth so information concerning the relative position of the earth, sun and asteroid must be included in the modeling.

Additionally, asteroids are not symmetric bodies and are often tumbling as they move. Since the surface is generally not uniform, the energy re-emitted is variable. All of these effects are unique to each asteroid so if asteroids are to be used care must be taken in selecting the specific asteroids to be considered.

d. IRAS Calibrations.

The initial calibration of data from IRAS proceeded along lines similar to those outlined above. The absolute calibration at $12\mu\text{m}$ was set so that the color corrected flux of α Tau at that wavelength was 448 Jy, in agreement with the ground based observations of Rieke, et al. (1984) at $10.6\mu\text{m}$ (Supplement, VI-20). The extrapolation of the ground based observations from $10.6\mu\text{m}$ to $12\mu\text{m}$ was done assuming that the energy distribution of α Tau followed that of a blackbody. α Tau was chosen because it was thoroughly measured by IRAS with a high signal to noise ratio and because it was a primary standard in the calibration work of Rieke et al.

Extrapolation from the $12\mu\text{m}$ to the 25 and $60\mu\text{m}$ wavelengths in the original calibration was begun by comparing models of stars with widely varying surface gravities and temperatures. It was concluded that the color differences for $[12\mu\text{m} - 25\mu\text{m}]$ and $[25\mu\text{m} - 60\mu\text{m}]$ are very similar for a wide range of surface gravities and temperatures. Based upon this result, a group of well

measured stars with physically simple behaviors were chosen as secondary calibration standards. Then, since the color differences for $[12\mu\text{m} - 25\mu\text{m}]$ and $[25\mu\text{m} - 60\mu\text{m}]$ were thought to be very similar for many different stars, the color differences of the Sun given by Vernazza, Avrett and Loeser (1976) were used as the average color difference for the chosen stars. These colors are:

$$[12\mu\text{m} - 25\mu\text{m}] = -0.03 \text{ mag}$$

$$[25\mu\text{m} - 60\mu\text{m}] = -0.03 \text{ mag}$$

and were used as the average color differences for the chosen stars.

The calibration at $100\mu\text{m}$ was made by transferring the stellar calibration to asteroids at 25 and $60\mu\text{m}$ and then extrapolating to $100\mu\text{m}$. Three asteroids, Hygiea, Bamberga and Europa, were used. Hygiea and Europa were each measured 10 times while Bamberga was scanned 20 times. For each of these crossings, a color temperature was calculated at $[25\mu\text{m} - 60\mu\text{m}]$ from the stellar calibrations. The calibration was then extrapolated to $100\mu\text{m}$ by assuming that the color temperature $[60\mu\text{m} - 100\mu\text{m}]$ was equal to the color temperature $[25\mu\text{m} - 60\mu\text{m}]$. From the assumed $[60\mu\text{m} - 100\mu\text{m}]$ color temperature, flux levels were then calculated. The average of the predicted $100\mu\text{m}$ fluxes served as the $100\mu\text{m}$ absolute calibration.

This process was checked by comparing the flux at $100\mu\text{m}$

for nine asteroids with the calculations of the "standard asteroid model" of Morrison(1973) and Jones and Morrison(1974). The model was adjusted to give the measured $60\mu\text{m}$ flux and $100\mu\text{m}$ fluxes were then predicted. The $100\mu\text{m}$ calibration was then modified so that the mean of the ratios of the observed flux to the model flux was equal to one.

The estimated accuracy of stellar plus asteroid calibration relative to the $10\mu\text{m}$ ground based calibration is estimated as 2% at $12\mu\text{m}$, 5% at 25 and $60\mu\text{m}$, and 10% at $100\mu\text{m}$. Sources of error include uncertainties in the stellar and asteroid models and scatter in the measurement of the stars chosen as standards.

II. FOURIER ANALYSIS OF THE IRAS BEAM PROFILES

a. Introduction.

Fourier analysis provides a method to check the effectiveness of the short wavelength blocking provided by the filters on the 60 and 100 μ m detectors. In image space, the passage of the signal through the system is the convolution of the telescope point spread function at the operating wavelength and the characteristic angular response of the detector system. In Fourier space the output of the system is the product of the Fourier transform of the point spread function and that of the angular response of the detector. The response of the ideal filter is a delta function; it lets the point spread function pass at only the wavelength of interest. In reality, filters have a passband characterized by cuton and cutoff wavelengths. A leak in the filter changes the response by allowing a signal to pass at wavelengths outside of the passband. This increases the power falling on the detector and causes overestimation of the flux received from a source.

If energy is entering the detector at spectral frequencies outside of the passband this energy will also show up at spatial frequencies outside of the characteristic spatial frequencies appropriate to the filter-telescope combination in Fourier space. The power spectrum is a measure of the power in a signal at each spatial frequency. For a star, which is a

point source, all the power in the signal should be found at spatial frequencies inside the passband of the filter-telescope combination and the amplitude of the power spectrum should fall smoothly from a maximum value located at 0 cycles/arcsec. When the power spectrum shows a tail extending past the limits of the passband in Fourier space or when the shape of the power spectrum does not fall in a smooth curve from a maximum at zero, it is a clear indication that one of two conditions is present: either the input signal has some structure or the filter is not true to its intended response.

b. Analysis of Beam Profile.

Evidence for the existence of a short wavelength leak can also be detected in image space. In theory, if the filters are working properly and the scanning rate of the satellite is highly linear, nearly the same spatial frequencies will be present in the flux regardless of the temperature of the source. If the filters have a short wavelength leak, sources with higher temperatures will contain more of the higher spatial frequencies than sources with cooler temperatures. This excess high spatial frequency will cause the beam profile of the hotter source to rise more rapidly than that of the cooler source. Although the effect is subtle, it is indicated at $100\mu\text{m}$, as can be seen by aligning and overplotting the beam profiles for sources with different

effective temperatures. This has been demonstrated in Figure 2 by overplotting the star α Boo ($T = 4500$ °K) and an asteroid, Hygiea ($T = 220$ °K) (Lebofsky et al., 1985).

In addition to the evidence for a short wavelength leak from beam profile overplots, the power spectrum (square modulus of the Fourier transform) of α Boo at $100\mu\text{m}$ also clearly shows a tail at high spatial frequencies ($s > 7$, where s is spatial frequency in units of inverse arcmin) (Figure 3). Both of these circumstances indicate that a more detailed analysis through Fourier methods will be profitable. First, both detector noise and non-linearity in the scanning rate of the telescope will be ruled out as significant sources for the high frequency tail. Then comparison of α Boo's power spectrum with the power spectrum of the idealized telescope and the noise will be used to provide an estimate of the magnitude of any leakage. With this information, a correction can be made to flux levels and a new calibration made.

c. Power Spectrum Analysis.

1) Power Spectra Calculation Using the Fast Fourier Transform.

The first step was to develop the tools to perform and understand the Fourier analysis. The power spectrum analysis was done using SUBROUTINE SPCTRM from Numerical Recipes by Press, et.al (1989). This subroutine gives a one-sided power

spectral density defined as:

$$P(f) = |H(f)|^2 + |H(-f)|^2$$

which for positive, real functions is :

$$P(f) = 2|H(f)|^2$$

where $H(f)$ is the Fourier transform calculated as:

$$H(f) = \int_{-\infty}^{\infty} h(t) e^{2\pi i f t} dt$$

with $h(t)$ as a function in the time domain. In accordance with Parseval's Theorem, the total power is then:

$$P_T = \int_{-\infty}^{\infty} |h(t)|^2 dt = \int_{-\infty}^{\infty} |H(f)|^2 df$$

and is the same whether it is computed in the time or frequency domain.

Since the beam profiles are a finite discrete data stream

and not a continuous function, the discrete Fourier transform is required and is defined as:

$$H_n = \sum_{k=0}^{N-1} h_k e^{2\pi i kn/N}$$

and the discrete analog to Parseval's Theorem is:

$$P_T = \sum_{k=0}^{N-1} |h_k|^2 = \frac{1}{N} \sum_{n=0}^{N-1} |H_n|^2$$

At the heart of the subroutine lies a routine for calculating the Fourier transform of a segment of data points. This Fourier transform routine returns values for certain spatial frequencies, however the given value is an average over some frequency bin and not exactly the value of the Fourier transform at that frequency. In fact, the values tend to leak over into other frequency bins since they fall off only as the frequency offset from the center frequency squared. This produces significant leakage between frequency bins which may extend past even the adjacent bins, contaminating the power estimate.

The use of a data windowing function can reduce this error. When a discrete number of points is sampled, the

actual process can be thought of as multiplying an infinite sequence of data points by a window function which has a value of one only during the duration of the scan and is zero elsewhere. The Fourier transform of this multiplication is actually the convolution of the data's transform with the window's transform. The rapid rise and fall of the window function introduces a significant component at high frequencies which causes leakage. This high frequency component can be reduced by using a window that does not rise and fall quite so rapidly. A number of such functions are available. The chosen window is the Parzen Window:

$$w_j = 1 - \left| \frac{j - \frac{1}{2}(N+1)}{\frac{1}{2}(N+1)} \right|$$

where N is the number of data points.

2) Power Spectra Calculations.

The source chosen for power spectra analysis was α Boo. α Boo is a bright (-3.15 mag at 10 μ m) and well understood star. Fortunately, six scans of α Boo taken at 1/8th the survey rate and intended for calibration and super-resolution work were available (Low, 1990). The selected scans of α Boo were made by detector 6 on the IRAS focal plane. Detector 6

was chosen because it was one of the quietest 100 μ m detectors (Supplement, IV-1) and because of its favorable location on the focal plane (Supplement, II-11). These scans were corrected for variations in the scanning rate caused by slowing as the satellite reversed its motion at the end of a scan and interpolated using a cubic spline routine. Finally, each was resampled prior to beginning this project.

The signal to noise level of these scans ranged from 3 to 8. In order to improve this ratio, the six scans were coadded. Alignment of two scans was achieved by computing the correlation (Press, et. al., 1989) and offsetting the second scan by the number of data points indicated by the location of the maximum in the correlation function. Additional scans were added to these two using the same process.

Once the coadding was complete, a power spectrum was calculated according to methods described in the previous section. This power spectrum is found at Figure 3.

An estimation of the power in the background noise was obtained by taking power spectra of scans across an empty segment of the sky made by detector 6. These data were handled identically to the regular signal-- interpolation using a cubic spline routine and resampling at the same rate as the original scans of α Boo. A number of these scans were run in order to preclude use of scans with either abnormally high or low noise levels. No significant difference was

found among any of the power spectra run from empty scans.

3) Analysis of Power Spectra.

A variety of disturbances caused by conditions in image space can alter the shape of the power spectrum at certain frequencies. The majority of these disturbances show up in the lower spatial frequencies; that is, they inject additional power into low frequencies. Discrepancies in the higher frequencies, which show up as a high frequency tail outside of the passband of the filter, are caused by one or a combination of three things: detector noise, a deviation from linearity in the reconstructed satellite scan rate, or a short wavelength leak in the blocking filters. Once the mechanics of determining the power spectrum were finished, the next step was to rule out sources for the high frequency tail ($s > 7$, Figure 3) other than a short wavelength leak. To do this it was necessary to show that the contributions to the high frequency tail from detector noise and scanning non-linearities were negligible.

Detector noise as the primary source for the high frequency tail can effectively be ruled out. By definition, detector noise is that signal level which is present regardless of whether a detector is crossing a source or not. As can be seen in Figure 4, a high frequency component ($s > 7$) is also visible in the noise. When the noise and source power spectra are overplotted (Figure 7), the noise is

clearly the dominant source of power in the signal at mid-frequencies ($4 < s < 7$) but inside the passband (set by the cuton frequency at a spatial frequency of $s < 3.4$) and out in the high frequency tail ($s > 7$), the power in the noise is at least one order of magnitude below the power in the source. Noise is therefore not a major source of the high frequency tail since the noise accounts for less than 10% of the signal at the spatial frequencies of interest.

A lack of linearity in the scan rate of the satellite as the primary source for the high frequency tail can also be ruled out quite easily. Since this non-linearity would affect the entire satellite, the high frequency tail should be seen at all wavelengths and equally for all spectral energy distributions. If the high frequency tail is not present in each band, or in all spectral energy levels, then non-linearity in the scanning rate of the satellite is not the source of the tail.

To verify linearity in the satellite scans, scans of α Boo at $60\ \mu\text{m}$ and scans of the much colder asteroid Hygiea at $100\ \mu\text{m}$ were obtained. Power spectra were computed and once again a small high frequency component (at $s > 7$) was seen outside the short wavelength cutoff (Figures 5 & 6). Overplotting the appropriate noise power spectra on the power spectra of these two sources showed however, that for colder sources or for hotter sources in the $60\ \mu\text{m}$ band both

tails could be accounted for by the noise. Since a significant high frequency tail exists only for the 100 μ m detections of a hot source, non-linearity as a source for the high frequency tail can be ruled out. Since noise has also been ruled out as a significant source for the high frequency tail at 100 μ m, it is safe to assume that the tail is evidence of a short wavelength leak in the 100 μ m detectors.

d. Estimation of the Magnitude of the Leak.

The last step is to determine the magnitude of the leak in the 100 μ m detectors. The first key point in this process is to determine the theoretically expected power spectrum for α Boo at 100 μ m.

In this case, the modulation transfer function (MTF) was used as an estimation of the expected response. The MTF is the factor which modulates the Optical Transfer Function (OTF). The OTF is the Fourier transform of the Point Spread Function (PSF). This choice is based upon the fact that the expected power spectrum is proportional to the square of the MTF where the MTF is calculated for a frequency of interest. Using the MTF for the cuton frequency gives the maximum permitted power. Since there is very little transmission at the cuton frequency, a better estimate of the size of any leak would be given by using the effective wavelength of the detector. The calculation of the MTF takes into account the fact that the aperture is obstructed--the secondary mirror

requires that the ideal telescope response be calculated for an annular aperture.

An MTF for the IRAS system was obtained from a program by Thomas E. Milner. This program computes the MTF by taking the Fourier transform of the autocorrelation of an annular aperture with the following characteristics:

Exit Pupil: 1.16mm
Central Obscuration: .488mm

as derived from data in the IRAS Explanatory Supplement. The cutoff spatial frequency for the passband is calculated as:

$$f_c = \frac{D}{\lambda} \frac{s}{z}$$

where D is the diameter of the exit pupil (1.16mm, Supplement, II-16) λ is the wavelength in question, z is the distance between the exit pupil and focal plane, (Supplement, II-16) and s is the measured plate scale (1.585 mm/arcmin, Supplement, II-8) at the focal plane. The MTF is normalized in amplitude by fitting it to the measured power spectrum from which the calculated noise levels have been subtracted. From this, it can be seen in Figure 7 that a significant amount of signal lies outside the intended passband ($s > 3.4$).

The three curves calculated above (the power spectra of the source and the noise, and the MTF) are overplotted in Figure 7. The leak may be seen by noting the significant high frequency tail in the measured data that extends horizontally far beyond the $65\mu\text{m}$ cutoff (3.3 cycles/arcmin) and is about one order of magnitude above the noise level. The power spectrum at $60\mu\text{m}$ shows no such feature (Figure 5), lending weight to the conclusion that its filters do not leak.

The area under the power spectrum curve and outside of the passband cutoff provides an estimate of the power which is being allowed to leak into the detectors. To estimate the amount of the leak, the power spectra of the original signal and the background noise were computed. Then the area inside the passband as defined by the MTF and the area under noise spectrum were subtracted from the original signal in Fourier space. The MTF used to calculate the size of the leak is the MTF at $100\mu\text{m}$ rather than the MTF at $65\mu\text{m}$ since $100\mu\text{m}$ is the effective wavelength of the detector. The remaining area under the power spectrum curve becomes an estimate of the power in the leakage and was compared with the area under the total power spectrum to yield a leakage measurement of 14.3% of the original signal. The minimum magnitude of the leak is computed by using the $65\mu\text{m}$ (cutoff) MTF and is 9.3%.

Uncertainties in the estimate of the leak arise from two causes: the uncertainty in the effective wavelength of the

leak between 3.5 and 4.5 μ m and possible errors in normalizing the leak to the high frequency tail in the total MTF. The first area contributes an uncertainty of about 15% in the estimated value, while the second contributes about 20%. The net uncertainty is 25%; i.e., the estimated leak for α Boo is $14.3 \pm 3.6\%$ of the measured signal.

e. Conclusions.

Fourier analysis of the 60 and 100 μ m signals from IRAS has successfully provided additional insight into the effectiveness of the filters used in the two bands. The 60 μ m filters show no evidence under Fourier analysis for any significant leakage and can therefore be used without correction. The 100 μ m beam profiles in image space and the power spectrum in frequency space clearly show evidence of a significant amount of high frequency input and therefore required further analysis.

Non-linearity in the satellite scan rates as a source for the higher spatial frequencies can be ruled out because the high frequency features are not found in other bands or in spectra taken from colder sources. Detector noise, while present, is not large enough to account for all the high frequency input at 100 μ m. The only remaining source for the high spatial frequencies is a short wavelength leak in the 100 μ m filters.

The amount of this leakage was determined by removing

the expected signal (determined as the MTF from the ideal telescope response) and the noise estimates from a power spectrum made from observation of α Boo taken by detector 6. From a measurement of the area then remaining under the power spectrum curve, the size of the leak appears to be about $14.3 \pm 3.6\%$ for stars with colors similar to that of α Boo. With this information, it is possible to correct measurements of stars similar to α Boo and produce a new stellar calibration at $100\mu\text{m}$.

III. CALIBRATION.

a. Introduction

The development of good stellar models out to wavelengths past $100\mu\text{m}$ now allows re-calibration of the IRAS flux levels directly from the ground-linked $12\mu\text{m}$ calibration using the well-understood physics of stellar atmospheres without recourse to asteroid models. At $100\mu\text{m}$, this new calibration will take into account corrections required by the discovery of a short wavelength leak. At 25 and $60\mu\text{m}$ as well as at $100\mu\text{m}$ it will indicate any discrepancies which might have arisen through the transfer of calibration to asteroids as well as serving as another check on previous calibrations.

b. Selection of Calibration Sources.

The first step in this process was the choice of standard stars. Since this calibration attempt is aimed at infrared wavelengths as long as $100\mu\text{m}$, the stars chosen must have low effective temperatures in order to have a good signal to noise ratio at long wavelengths. On the other hand, very late stars often have complicated spectra and show variability. With these criteria in mind, a search of the Yale Bright Star Catalog produced a list of 48 stars with simple spectra, constant output, and relatively strong fluxes at infrared wavelengths.

Next, the measured IRAS flux from the Faint Source Catalog for these stars at all four wavelengths was

requested. The Faint Source Catalog data were chosen over that of the Point Source Catalog since the processing of the Faint Source Catalog was designed to provide maximum accuracy in flux measurements for sources with a signal to noise ratio less than 10. Of the 48 original stars, 33 had entries in the Faint Source Catalog. One of these, δ And was rejected completely because of a strong excess at both 60 and 100 μ m. The remaining 32 were used at both 25 and 60 μ m.

At 100 μ m, the criteria for inclusion became more rigorous. The 32 chosen stars were screened and 22 of the original stars were rejected. The status and criteria for rejection of each of the chosen stars is recorded in Table 1. Two stars were rejected because their effective temperatures were too much higher than that of α Boo so that leak corrections could not be accurately made. α Ari was rejected because of an apparent excess at 100 μ m. Examination of the Sky Flux plates showed that it is located in a heavy patch of infrared cirrus which has contaminated its measurements. The rest of the 22 rejected stars were rejected because of lack of a signal to noise estimate. The remaining smaller group of ten bright K giants had no known variability, no far infrared excess, no known spectral features longward of 10 μ m and a signal-to-noise ratio higher than 4.6 (the signal-to-noise ratio of α Tau).

c. Re-calibration.

1) Corrections to IRAS Data.

The first step in the re-calibration of IRAS flux levels was to make the required corrections to quoted flux levels. Two corrections have been made to these measurements. The first was to correct the 100 μ m measurements for the 14.3% leak identified earlier in this research. The size of the short wavelength leak could depend significantly on the temperature of the source. Since the leakage estimate was calculated from the beam profile of α Boo, only stars with effective temperatures similar to that of α Boo were corrected and used for the 100 μ m calibration.

The other adjustment is a color correction. The spectral response of each band is quite broad. Therefore, the measured flux will depend on the intrinsic energy distribution of the source. The Supplement explains that the flux values given in the IRAS data base are those of a source with an energy distribution such that:

$$f_c \propto \nu^{-1}$$

Since stars are hot blackbodies, each value is corrected according to the formula:

$$f_v(\text{actual}) = \frac{f_v(\text{quoted})}{K}$$

using the values for K given in Table VI.C.6, Main Explanatory Supplement where K is calculated as:

$$K = \frac{[\int (\frac{f_v}{f_{v_0}}) [\text{actual}] R_v dv]}{[\int (\frac{f_v}{f_{v_0}}) [\text{quoted}] R_v dv]}$$

and R_v is the relative system response given in Table II.C.5 of the Supplement.

The calibration of the Faint Source Catalog is directly tied to the absolute calibration of the Point Source Catalog at $12\mu\text{m}$. The Faint Source Catalog was calibrated by comparing 6,007 sources detected in both catalogs and lying within limits set to exclude sources which were either near the lower threshold for the Point Source Catalog or bright enough to induce a nonlinear response from the feedback resistors. Initially, the chosen sources were compared by

taking the ratio of the flux measurement in the Faint Source Catalog to that in the Point Source Catalog, weighted according to the flux value in the Faint Source Catalog:

$$\frac{F_v(FSC)}{F_v(PSC)}$$

and calculating the mean and forcing it to unity. Adjustments to this calibration were made in order to account for the feed back resistor characteristics and the mean ratio was recomputed and forced to unity to complete the calibration.

2) Stellar Models.

The next step was to find models for the stellar atmospheres of these stars. The models chosen were those of Kurucz (1991) and included flux calculations from approximately .1 to 160 μ m for effective temperatures from 3500 to 50,000 $^{\circ}$ K and log g from 0 to 5. None of these models predicted any unusual spectral features at long wavelengths; however, there is some deviation from a pure blackbody function, indicating the presence of some frequency dependent opacity.

The models used in the initial IRAS calibration (Gustafsson, et al., 1975; Kurucz, 1979; Bell, 1984)

predicted that the $[12\mu\text{m} - 25\mu\text{m}]$ and $[25\mu\text{m} - 60\mu\text{m}]$ colors were the same for a wide range of temperatures and surface gravities. This allowed the $[12\mu\text{m} - 25\mu\text{m}]$ and $[25\mu\text{m} - 60\mu\text{m}]$ colors to be determined by measurements of the Sun. The original $100\mu\text{m}$ calibration was tied to this by assuming the $[60\mu\text{m} - 100\mu\text{m}]$ color was equal to the $[25\mu\text{m} - 60\mu\text{m}]$ color determined for the asteroids from the stellar calibration.

The new stellar atmosphere models do not support these assumptions. Table 2 provides a comparison. The major differences between the new stellar models and the assumptions that went into the initial IRAS calibrations are that the $[12\mu\text{m} - 25\mu\text{m}]$ and $[25\mu\text{m} - 60\mu\text{m}]$ colors are not equal and these colors are much larger than the -0.03 mag determined from the work of Vernazza, Avrett, and Loeser (1976) on the Sun.

3) Calculation of Correction Factors.

The last step in deriving a new calibration was to apply the new models to the corrected IRAS data. Initially, the stellar models were interpolated between 10 and $160\mu\text{m}$ in order to get a predicted flux at intervals of one μm . The program used for this was a polynomial interpolation routine POLINT from Numerical Recipes, Press, et al. (1989).

Finally, the models were anchored to the absolute calibration by forcing the predicted $12\mu\text{m}$ flux to equal the measured $12\mu\text{m}$ color-corrected IRAS flux. The model

predictions at 25, 60, and 100 μ m were then calculated and compared to the corrected IRAS measurements at the same wavelength. The results are summarized in Table 3. The magnitude calculations follow those of the IRAS Explanatory Supplement with $f(0.00)$ set at 28.3, 6.73, 1.19 and .43 Jy at 12, 25, 60 and 100 μ m.

d. Conclusions.

Table 7 shows the results of this new calibration at 25, 60 and 100 μ m. The calibration began with comparison of the fluxes predicted by the models with the corrected flux measurements of the stars chosen from the Faint Source Catalog. At 25 μ m the measured IRAS fluxes are high by 13.5%, with a sample standard deviation of 3.5%. This distribution is plotted in Figure 8. The uncertainty (standard deviation of the mean) is .6%. When combined quadratically with the 3% uncertainty in the ground-based calibrations of Rieke, et al., the new calibration at 25 μ m has a nominal error of 3.1%. This estimate does not include systematic uncertainties in the stellar models. Detailed information on the predicted and measured fluxes at 25 μ m and the [12 μ m - 25 μ m] colors is in Table 4.

At 60 μ m the discrepancy between the measured and predicted fluxes was estimated using a noise weighted average. The IRAS measurements are high by 5% and the uncertainty in this value, calculated as the standard

deviation of the mean, is 1.8%. This distribution is plotted in Figure 9. Combined with the uncertainty in the ground based observations, the nominal overall uncertainty at $60\mu\text{m}$ is 3.5%. Detailed information on predicted and measured magnitudes and $[12\mu\text{m} - 60\mu\text{m}]$ colors is in Table 5.

Calibrations at $100\mu\text{m}$ proceeded along two separate paths. Nine of the ten stars used (Table 6) were weighted by noise (the highest signal to noise ratio in this group was 12) and averaged. The tenth star, α Boo, was singled out by its high signal to noise ratio (40) as a check on the average computed from the other nine stars. At $100\mu\text{m}$, the IRAS measurements of the nine weighted stars are too high by an average of 2.9%. The uncertainty is 4.6%. The measurement of α Boo is low by 3.4% with an uncertainty of 2.7%.

Combining these two measurements (straight averaging) yields an average of 0.3% low; we take the uncertainty to be 4%. Combining this error quadratically with the 3% uncertainty in the calibration at $10\mu\text{m}$ and the 3.6% uncertainty in the estimate of the leak, the total uncertainty is 6.2%. The results for $100\mu\text{m}$ are in Table 6.

IV. CONCLUSIONS

Fourier analysis of the IRAS beam profiles at 60 and 100 μ m shows the clear presence of a high spatial frequency tail in the output of the 100 μ m detectors. Detector noise as a source for this tail was ruled out by Fourier analysis of empty scans; although a tail is present in the noise spectrum, its magnitude is not large enough to account for the tail found in the scans across a source. Non-linearity in the satellite scanning is also not the source of the tail since a similar tail is not found at all wavelengths or spectral energy distributions.

Since all other known possible causes for this tail have been ruled out, it is safe to conclude that it is evidence of a short wavelength leak. An estimate of the magnitude of the leak was made by subtracting the power spectrum of the noise and the theoretical power spectrum from the power spectrum of the source and then computing the area remaining under the curve. This process yielded a leakage estimate of $14.3 \pm 3.6\%$ of the flux for sources with effective temperatures near that of α Boo.

Once the size of the leak was known, it was possible to re-calibrate the flux measurements in all four bands. Measurements in all four bands were obtained for a carefully chosen group of 33 bright, constant, and "well-behaved" stars from the Faint Source Catalog. These measurements were corrected for color in all four bands and for the leak at

100 μ m. In contrast to the initial piecewise calibrations, models were used to calibrate the flux in each band directly from the 12 μ m measurements. The 12 μ m measurements are in turn linked to the ground-based calibrations of Rieke, et al.(1984) at 10.6 μ m.

Re-calibration of the 25 μ m measurements shows that the current IRAS calibrations overestimate the 25 μ m fluxes by 13.5%. Using this as the basis for a new calibration at 25 μ m, the nominal estimated uncertainty in measurements at 25 μ m is 3.1%. Calculations at 60 μ m show that the IRAS measurements are overestimated by 5% with a nominal uncertainty of 3.5%

At 100 μ m ten stars were chosen from the original 33. A noise-weighted average of nine of these stars showed that the original IRAS calibrations overestimated the flux by 2.9%. The tenth star, α Boo, singled out for separate calculations because of its high signal-to-noise ratio, was used to check this average and proved to be underestimated by 3.4%. This agreement supports the conclusion that the flux is indeed underestimated. The average of these two (an underestimation of the flux by 0.3%) is the basis for a new calibration at 100 μ m. The nominal estimation of the uncertainty of the calibration at 100 μ m is 6.2%.

APPENDIX A: TABLES

Table 1: Status of Calibration Stars

	25 μ m	60 μ m	100 μ m	Comments:
α Car	Y	Y	N	Temperature too high
α CMi	Y	Y	N	"
α Phe	Y	Y	N	No SNR
β Cet	Y	Y	N	"
β Gem	Y	Y	Y	
α UMa	Y	Y	Y	
θ Cen	Y	Y	N	Low SNR
τ Pup	Y	Y	N	No SNR
Ψ UMa	Y	Y	N	"
α Boo	Y	Y	Y	
α Ari	Y	Y	N	Excess at 100um
ν Hyd	Y	Y	N	No SNR
ϵ Crv	Y	Y	N	"
α Ser	Y	Y	N	"
β Ophi	Y	Y	N	"
δ And	N	N	N	Excess at 60, 100um
ϵ Car	Y	Y	Y	
α Tuc	Y	Y	N	No SNR
43 Eri	Y	Y	N	"
31 Lyn	Y	Y	N	"
μ Hyd	Y	Y	N	"
β UMa	Y	Y	Y	
γ And	Y	Y	Y	
α Hya	Y	Y	Y	
π Her	Y	Y	N	Low SNR
α Tra	Y	Y	N	No SNR
ϕ Lup	Y	Y	N	"
α Tau	Y	Y	Y	
ϵ Lep	Y	Y	N	Low SNR
σ Pup	Y	Y	N	No SNR
π Pup	Y	Y	N	"
β Ara	Y	Y	N	"
α Lyn	Y	Y	Y	

Table 2: Comparison of Colors Derived from New

Non-LTE Stellar Atmosphere Models with
Those Used in the Initial Calibrations

New Models:

	[12 μ m - 25 μ m] (mag)	[25 μ m - 60 μ m] (mag)	[60 μ m - 100 μ m] (mag)
F0 II	-.164	.046	-.019
K0 III	-.164	.046	-.019
K3 I	-.155	.057	-.017
K5 III	-.155	.057	-.017
K7 III	-.155	.057	-.017

Original Model Predictions:*

[12 μ m - 25 μ m]	-0.03 mag
[25 μ m - 60 μ m]	-0.03 mag

*assumed to be equal for all spectral types and luminosity classes.

*asteroid [60 μ m - 100 μ m] color temperatures were assumed to be equal to their color temperatures at [25 μ m - 60 μ m].

Table 3: Predicted and Measured Flux

	Wavelength (μm)	Model (Jy)	IRAS (Jy)	Model/IRAS
α Car				
	12.		108.04	
	25.	22.09	25.85	.854
	60.	4.08	4.07	1.002
	100.	1.45	1.28	1.130
α CMi				
	12.		57.97	
	25.	11.85	13.38	.886
	60.	2.19	2.27	.963
	100.	0.78	0.56	1.375
α Phe				
	12.		39.18	
	25.	8.01	9.34	.858
	60.	1.48	1.41	1.045
	100.	0.52	0.84	.627
β Cet				
	12.		43.77	
	25.	8.95	9.49	.943
	60.	1.65	1.55	1.061
	100.	0.58	1.80	.326
β Gem				
	12.		89.01	
	25.	18.20	20.65	.881
	60.	3.36	3.74	.898
	100.	1.19	1.18	1.015
α UMa				
	12.		59.58	
	25.	12.18	14.17	.859
	60.	2.25	2.34	.959
	100.	0.80	0.81	.985

Table 3 (con't): Predicted and Measured Flux

	Wavelength (μm)	Model (Jy)	IRAS (Jy)	Model/IRAS
θ Cen				
	12.		41.28	
	25.	8.44	9.66	.873
	60.	1.56	1.46	1.068
	100.	0.55	0.73	.762
τ Pup				
	12.		23.41	
	25.	4.79	5.98	.800
	60.	0.88	0.90	.984
	100.	0.31	0.64	.493
Ψ UMa				
	12.		21.37	
	25.	4.37	5.19	.842
	60.	0.81	0.87	.930
	100.	0.29	0.38	.750
α Boo				
	12.		538.94	
	25.	110.17	114.00	.966
	60.	20.33	19.63	1.036
	100.	7.22	6.29	1.147
α Ari				
	12.		59.69	
	25.	12.20	14.29	.854
	60.	2.25	2.13	1.057
	100.	0.80	1.38	.580
ν Hyd				
	12.		25.24	
	25.	5.16	5.83	.885
	60.	0.95	0.98	.972
	100.	0.34	0.48	.699

Table 3 (con't): Predicted and Measured Flux

	Wavelength (μm)	Model (Jy)	IRAS (Jy)	Model/IRAS
ϵ Crv				
	12.		30.49	
	25.	6.23	7.16	.871
	60.	1.15	1.32	.874
	100.	0.41	1.01	.405
α Ser				
	12.		28.82	
	25.	5.89	7.17	.821
	60.	1.09	1.05	1.034
	100.	0.39	0.67	.573
β Ophi				
	12.		26.74	
	25.	5.51	6.25	.881
	60.	1.03	1.06	.965
	100.	0.37	2.55	.143
ϵ Car				
	12.		173.94	
	25.	35.85	44.17	.812
	60.	6.68	7.29	.916
	100.	2.38	1.75	1.361
α Tuc				
	12.		43.20	
	25.	8.91	10.45	.852
	60.	1.66	1.75	.947
	100.	0.59	0.56	1.048
43 Eri				
	12.		20.20	
	25.	4.16	5.06	.823
	60.	0.78	0.69	1.130
	100.	0.28	0.38	.720

Table 3 (con't): Predicted and Measured Flux

	Wavelength (μm)	Model (Jy)	IRAS (Jy)	Model/IRAS
31 Lyn				
	12.		19.39	
	25.	4.00	4.64	.861
	60.	0.74	0.75	.993
	100.	0.26	0.95	.278
μ Hyd				
	12.		22.80	
	25.	4.70	5.37	.875
	60.	0.88	0.97	.902
	100.	0.31	1.20	.260
β UMa				
	12.		114.65	
	25.	23.63	27.48	.860
	60.	4.40	4.47	.985
	100.	1.57	1.42	1.106
γ And				
	12.		70.39	
	25.	14.51	17.06	.850
	60.	2.70	2.78	.971
	100.	0.96	0.73	1.321
α Hyd				
	12.		108.73	
	25.	22.41	24.16	.927
	60.	4.18	3.99	1.047
	100.	1.49	1.00	1.485
π Her				
	12.		33.49	
	25.	6.90	7.86	.878
	60.	1.29	1.32	.976
	100.	0.46	0.47	.978

Table 3 (con't): Predicted and Measured Flux

	Wavelength (μm)	Model (Jy)	IRAS (Jy)	Model/IRAS
α TrA				
	12.		104.72	
	25.	21.58	24.03	.898
	60.	4.02	4.18	.963
	100.	1.43	1.93	.740
ϕ Lup				
	12.		35.41	
	25.	7.30	8.47	.862
	60.	1.36	1.33	1.020
	100.	0.48	1.88	.257
α Tau				
	12.		450.00	
	25.	92.75	108.07	.858
	60.	17.29	18.87	.916
	100.	6.15	4.64	1.326
ϵ Lep				
	12.		39.68	
	25.	8.18	9.30	.879
	60.	1.52	1.53	.998
	100.	0.54	0.46	1.190
σ Pup				
	12.		49.62	
	25.	10.23	12.23	.836
	60.	1.91	1.85	1.030
	100.	0.68	4.2788	.158
π Pup				
	12.		95.56	
	25.	19.70	23.89	.824
	60.	3.67	3.90	.942
	100.	1.31	2.77	.471

Table 3 (con't): Predicted and Measured Flux

	Wavelength (μm)	Model (Jy)	IRAS (Jy)	Model/IRAS
β Ara				
	12.		45.10	
	25.	9.30	11.09	.837
	60.	1.73	2.16	.801
	100.	0.62	2.29	.269
α Lyn				
	12.		59.42	
	25.	12.25	14.13	.867
	60.	2.28	2.35	.970
	100.	0.81	0.82	.990

Table 4: 25 μ m Magnitudes and Colors

Name	Magnitudes			[12 μ m - 25 μ m] Colors	
	Model	IRAS	Difference	Model	IRAS
α Car	-1.29	-1.46	.17	-.164	.007
α CMa	-0.61	-0.75	.14	"	-.032
α Phe	-0.19	-0.36	.17	"	.002
β Cet	-0.31	-0.37	.06	"	-.100
β Gem	-1.08	-1.22	.14	"	-.027
α UMa	-0.64	-0.81	.17	"	.000
θ Cen	-0.25	-0.39	.15	"	-.017
τ Pup	0.37	0.13	.24	"	.078
Ψ UMa	0.47	0.28	.19	"	.023
α Boo	-3.04	-3.07	.04	"	-.164
α Ari	-0.65	-0.82	.17	"	.007
ν Hyd	0.29	0.16	.13	"	-.032
ϵ Crv	0.08	-0.07	.15	"	-.014
α Ser	0.15	-0.07	.21	"	.049
β Ophi	0.22	0.08	.14	-.155	-.018
ϵ Car	-1.82	-2.04	.23	"	.071
α Tuc	-0.30	-0.48	.17	"	.018
43 Eri	0.52	0.31	.21	"	.057
31 Lyn	0.57	0.40	.16	"	.007
μ Hyd	0.39	0.25	.15	"	-.011
β UMa	-1.36	-1.53	.16	"	.009
α Hyd	-1.31	-1.39	.08	"	-.074
π Her	-0.03	-0.17	.14	"	-.015
α TrA	-1.27	-1.38	.12	"	-.039
ϕ Lup	-0.09	-0.25	.16	"	.007
α Tau	-2.85	-3.01	.17	"	.011
ϵ Lep	-0.21	-0.35	.14	"	-.015
σ Pup	-0.45	-0.65	.19	"	.039
π Pup	-1.17	-1.38	.21	"	.054
β Ara	-0.35	-0.54	.19	"	.037
α Lyn	-0.65	-0.81	.16	"	.000

Table 5: 60 μ m Magnitudes and Colors

Name	Magnitudes			[12 μ m - 60 μ m] Colors	
	Model	IRAS	Difference	Model	IRAS
α Car	-1.34	-1.34	.00	-.118	-.120
α CMa	-0.66	-0.70	.04	"	-.077
α Phe	-0.24	-0.19	-.05	"	-.166
β Cen	-0.36	-0.29	-.07	"	-.185
β Gem	-1.13	-1.24	.12	"	-.001
α UMa	-0.69	-0.74	.05	"	-.072
θ Cen	-0.29	-0.22	-.07	"	-.189
τ Pup	0.32	0.31	.18	"	-.100
Ψ UMa	0.42	0.34	.08	"	-.039
α Ari	-0.69	-0.63	-.06	"	-.17
ν Hyd	0.24	0.21	.03	"	-.087
ε Crv	0.04	-0.11	.15	"	.028
α Ser	0.10	0.14	-.04	"	-.154
β Ophi	0.16	0.12	.04	-.098	-.060
ε Car	-1.87	-1.97	.10	"	-.003
α Tuc	-0.36	-0.42	.06	"	-.039
43 Eri	0.46	0.60	-.14	"	-.230
31 Lyn	0.51	0.50	.01	"	-.091
μ Hyd	0.33	0.22	.11	"	.014
β UMa	-1.42	-1.44	.02	"	-.082
γ And	-0.89	-0.92	.03	"	-.067
α Hyd	-1.36	-1.31	-.05	"	-.148
π Her	-0.09	-0.11	.02	"	-.072
α TrA	-1.32	-1.36	.04	"	-.057
ϕ Lup	-0.15	-0.12	-.03	"	-.120
α Tau	-2.91	-3.00	.09	"	-.003
ε Lep	-0.27	-0.27	.00	"	-.096
σ Pup	-0.51	-0.48	-.03	"	-.130
π Pup	-1.22	-1.29	-.07	"	-.034
β Ara	-0.41	-0.65	.24	"	.143
α Lyn	-0.71	-0.74	.03	"	-.065

Table 6: 100 μ m Magnitudes and Colors

Name	Magnitudes			[12 μ m -100 μ m] Colors	
	Model	IRAS	Difference	Model	IRAS
β Gem	-1.11	-1.09	-.02	-.137	-.152
α UMa	-0.67	-0.69	.02	"	-.120
α Boo	-3.06	-2.91	-.15	"	-.286
ϵ Car	-1.86	-1.52	-.33	"	-.450
β UMa	-1.40	-1.29	-.11	-.115	-.224
γ And	-0.87	-0.57	-.30	"	-.417
α Hyd	-1.35	-0.92	-.43	"	-.544
α Tau	-2.89	-2.58	-.31	"	-.422
ϵ Lep	-0.25	-0.06	-.19	"	-.304
α Lyn	-0.69	-0.70	.01	"	-.104

Table 7: Summary of Calibration Corrections*

Band	Correction
25 μ m	-13.5%
60 μ m	- 5.0%
100 μ m	+ 0.3%

*Color corrected IRAS measurements should be decremented (-)
or increased (+) by the amount indicated

APPENDIX B: FIGURES

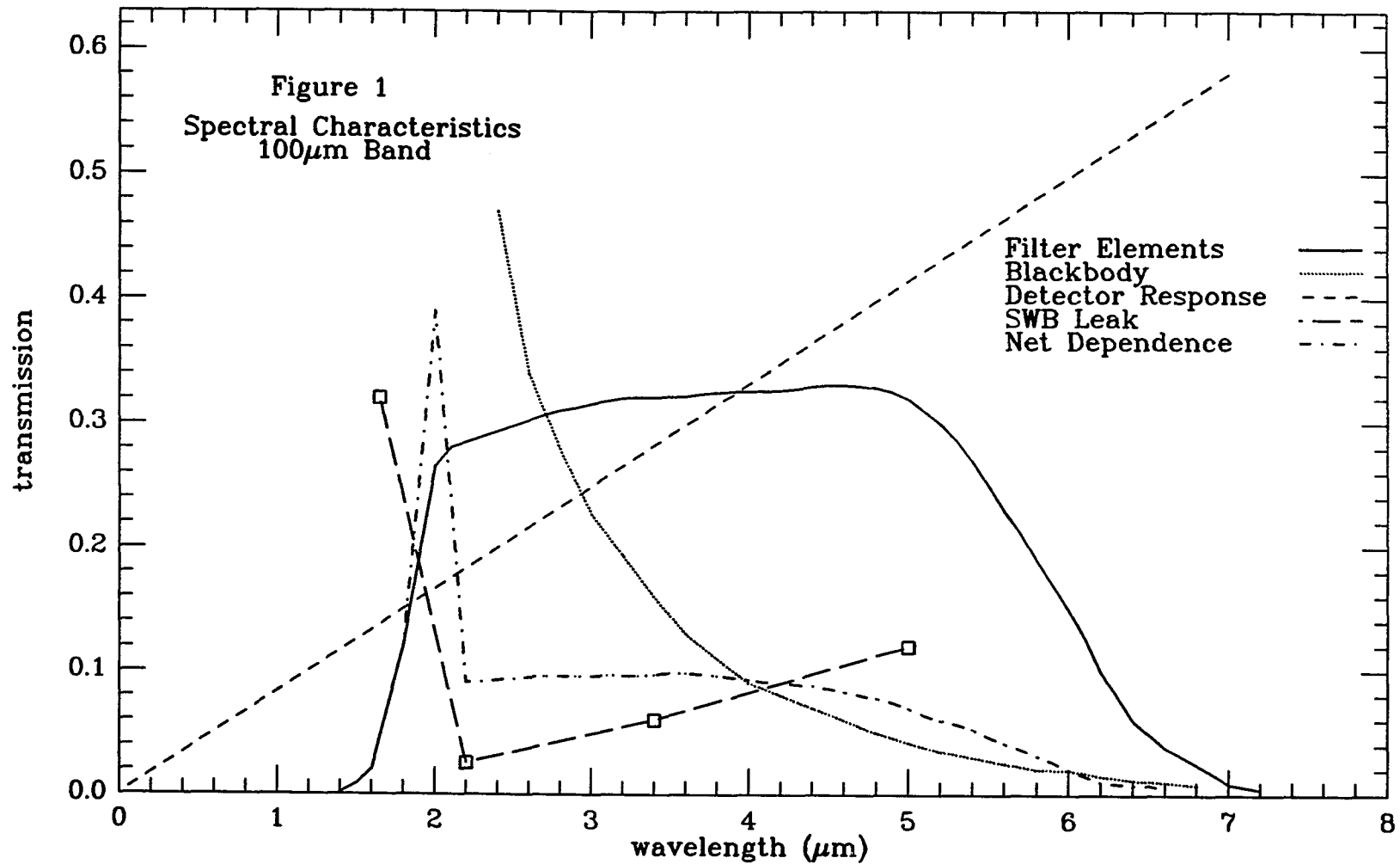


Fig. 1 Shows the spectral characteristics of a possible short wavelength leak in the 100 μ m filters. According to this, the effective wavelength of the leak would be 3.5 μ m, however scattering by the diamond powder may have biased the leak to wavelengths as long as 4.5 μ m.

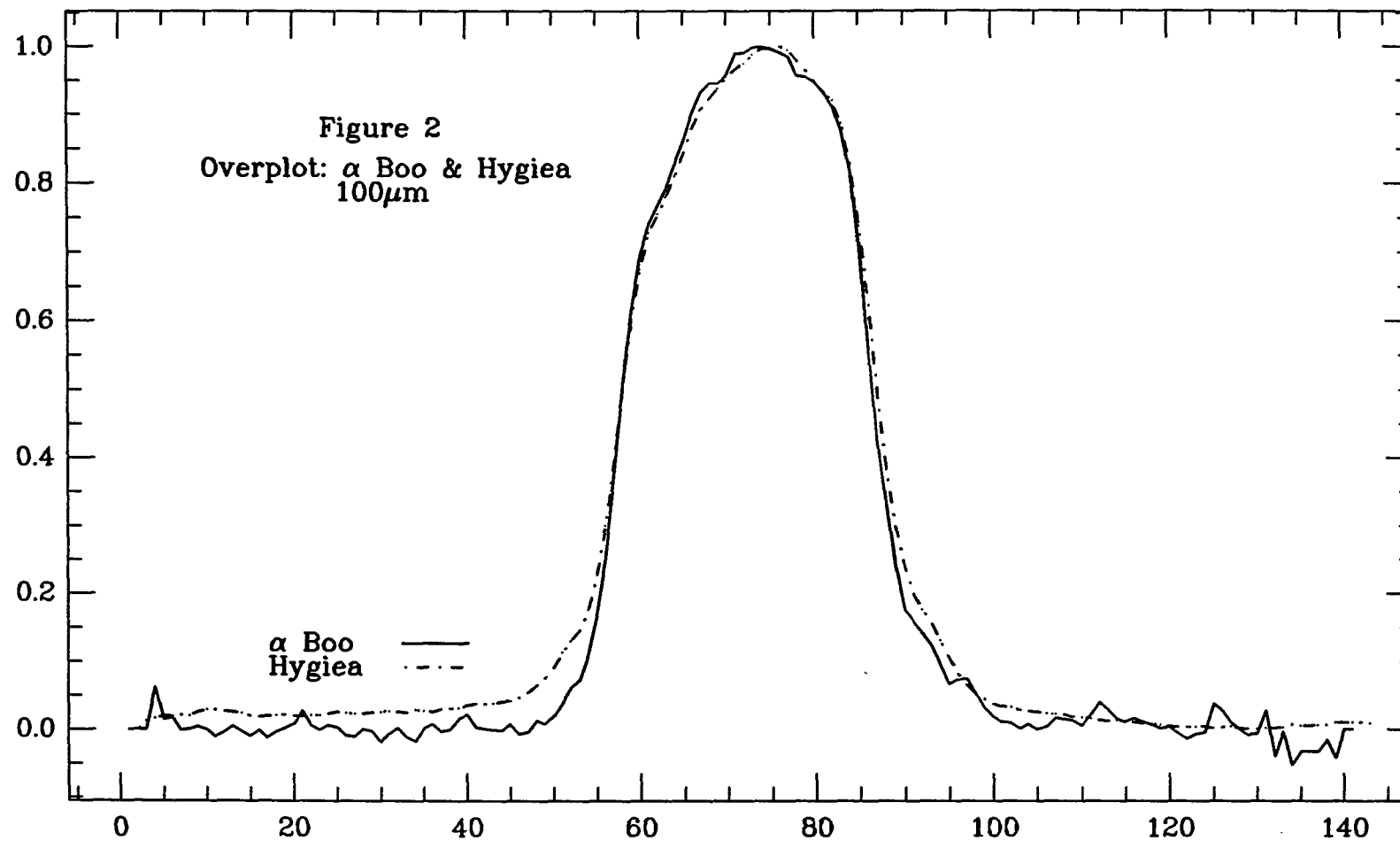


Fig. 2 Overplot of hot (α Boo) and cold (Hygiea) sources showing that the beam profile of the hot source rises faster than the beam profile of the cold source. This demonstrates the presence of higher spatial frequencies in the hotter source, indicating the possible presence of a short wavelength leak.

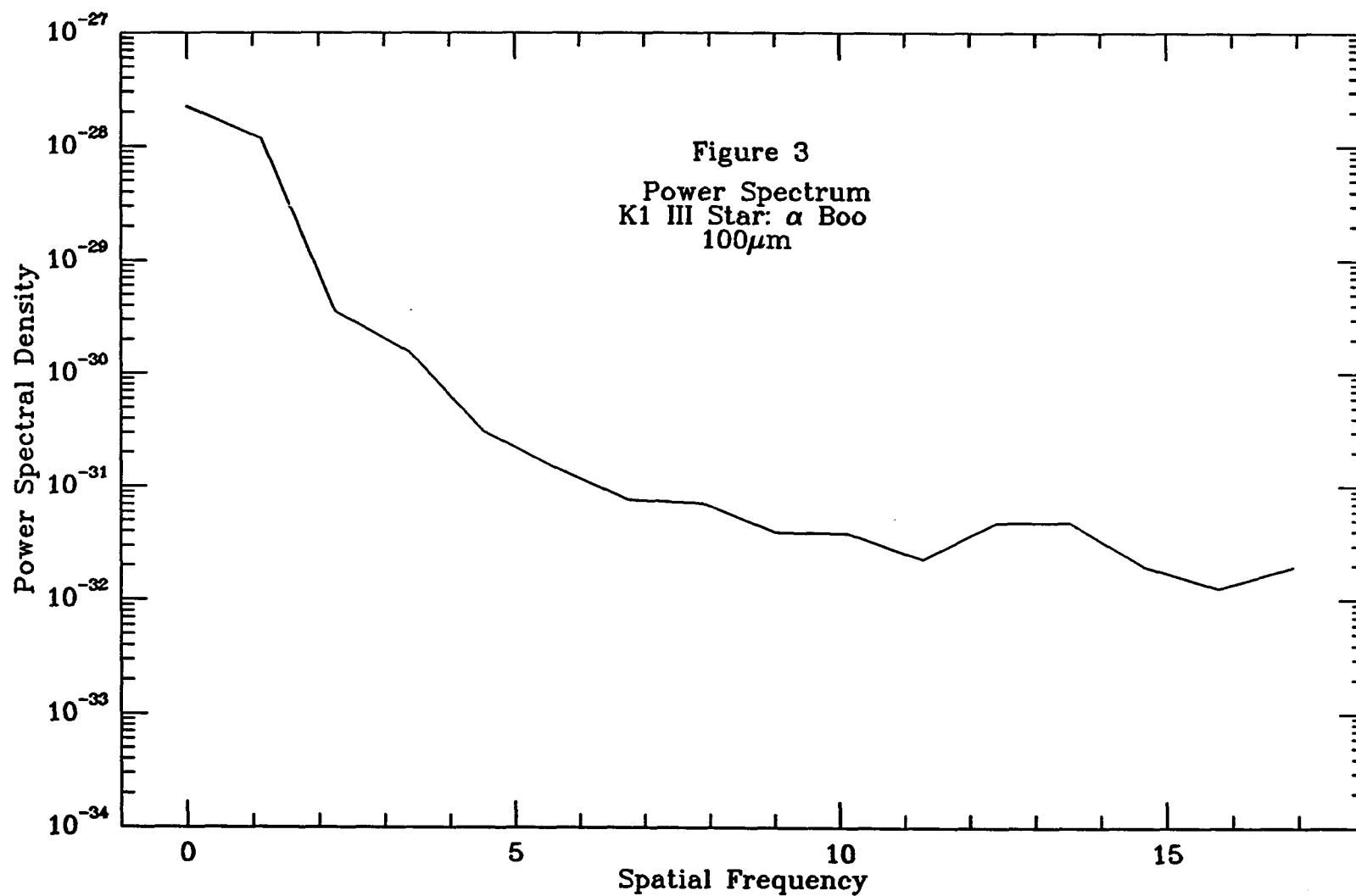


Fig. 3 Power spectrum of α Boo. Note the extension of the power spectrum into the higher spatial frequencies ($s > 7$).

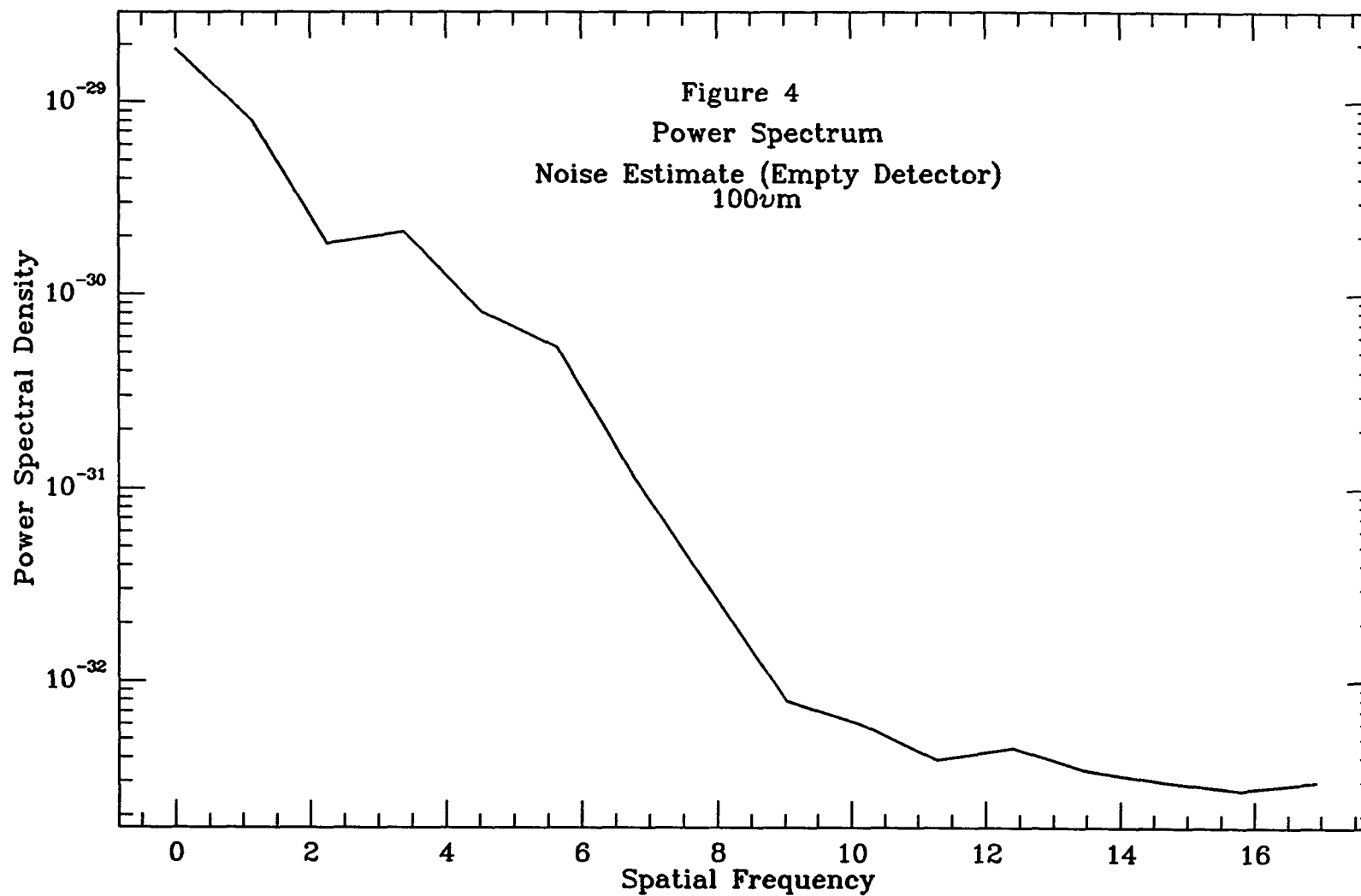


Fig. 4 Power spectrum of the noise in IRAS detector 6.

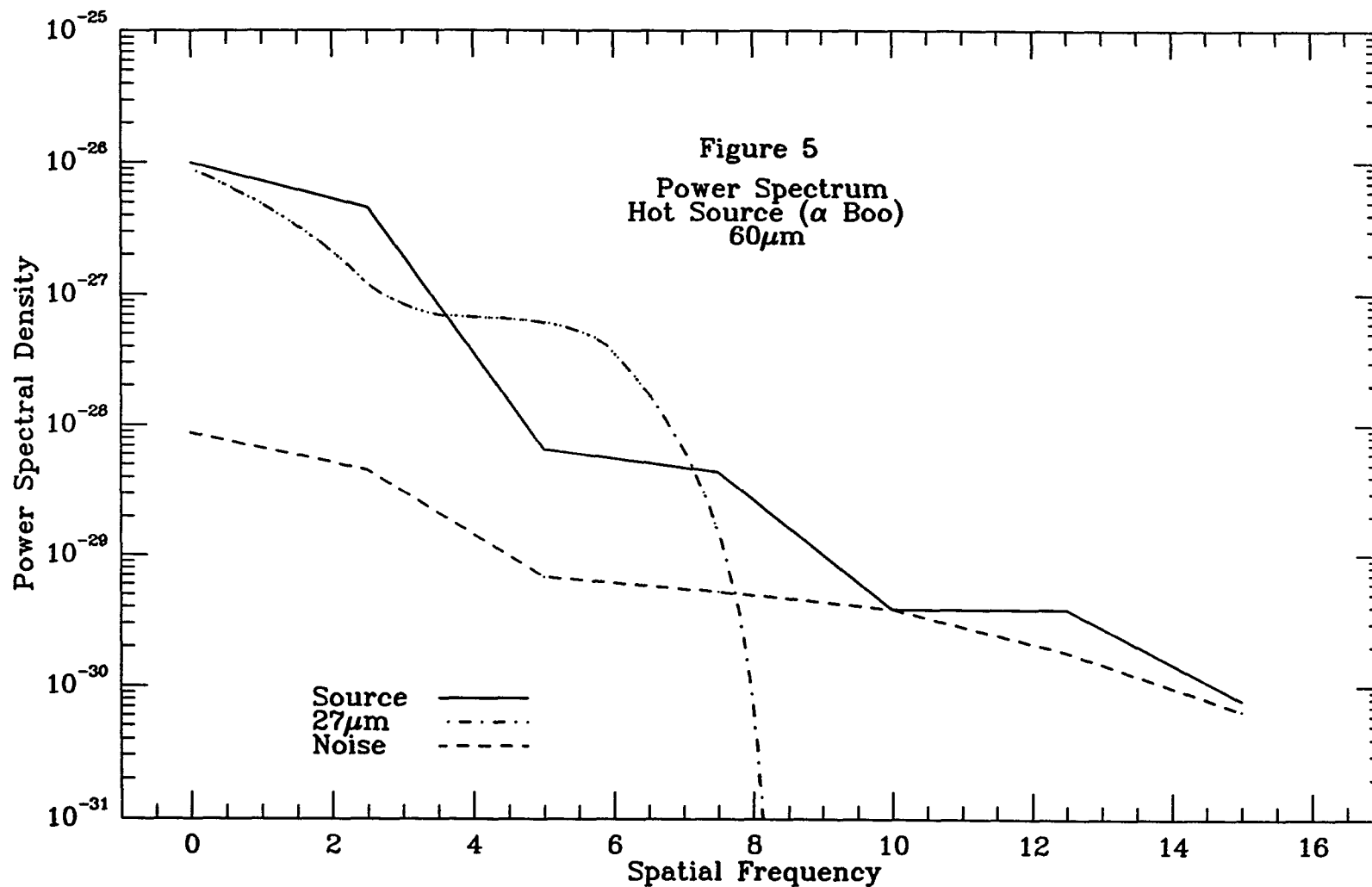


Fig. 5 Overplot of noise and short wavelength cutoff on the power spectrum of α Boo at $60\mu\text{m}$. Note that outside of the passband (dot-dash curve) the high frequency tail is almost entirely accounted for by the power in the noise.

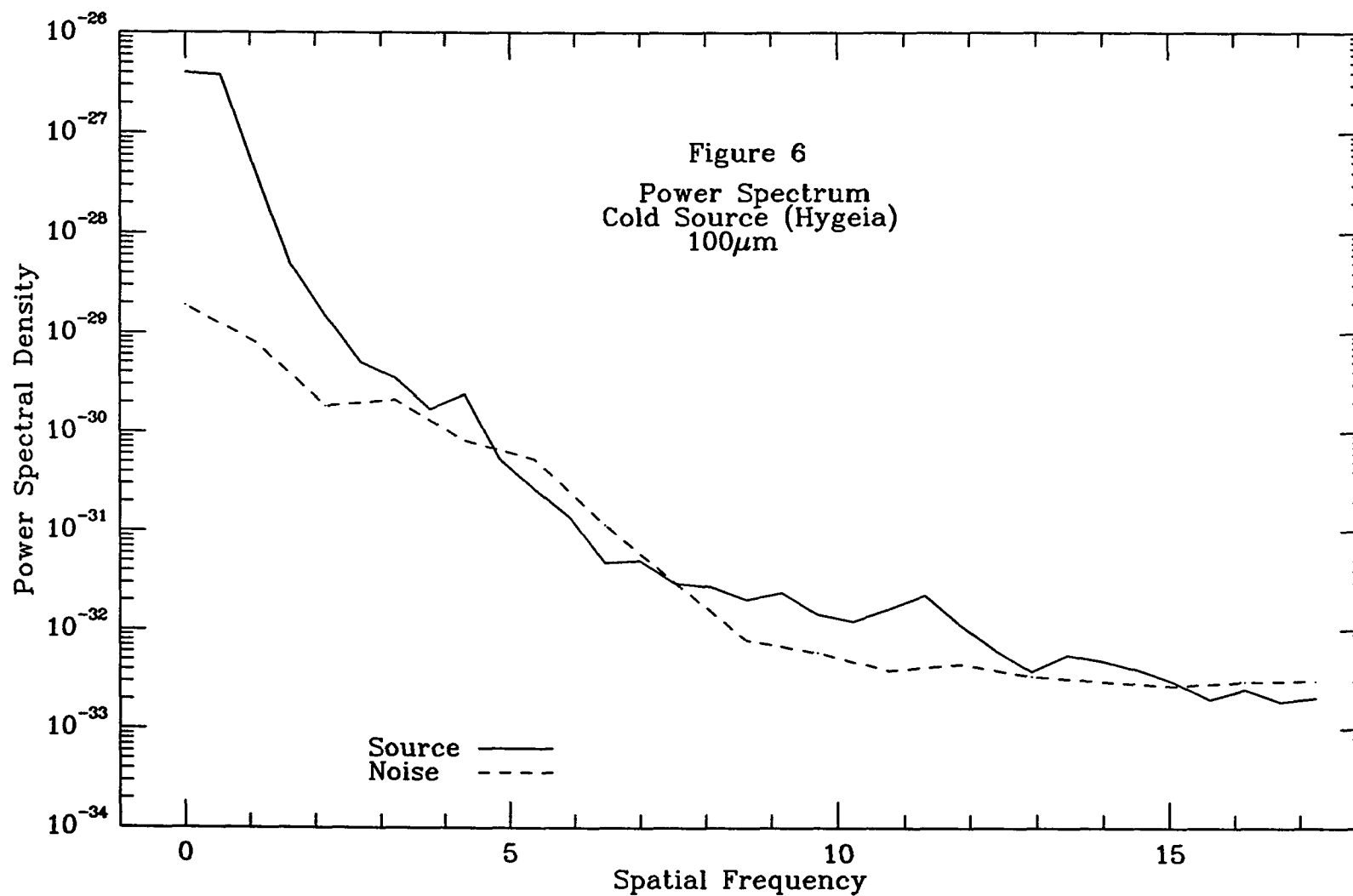


Fig. 6 Power spectrum of the asteroid Hygeia with a detector 6 noise power spectrum overplotted (dashed curve). Note that the high frequency tail is accounted for by the power in the noise.

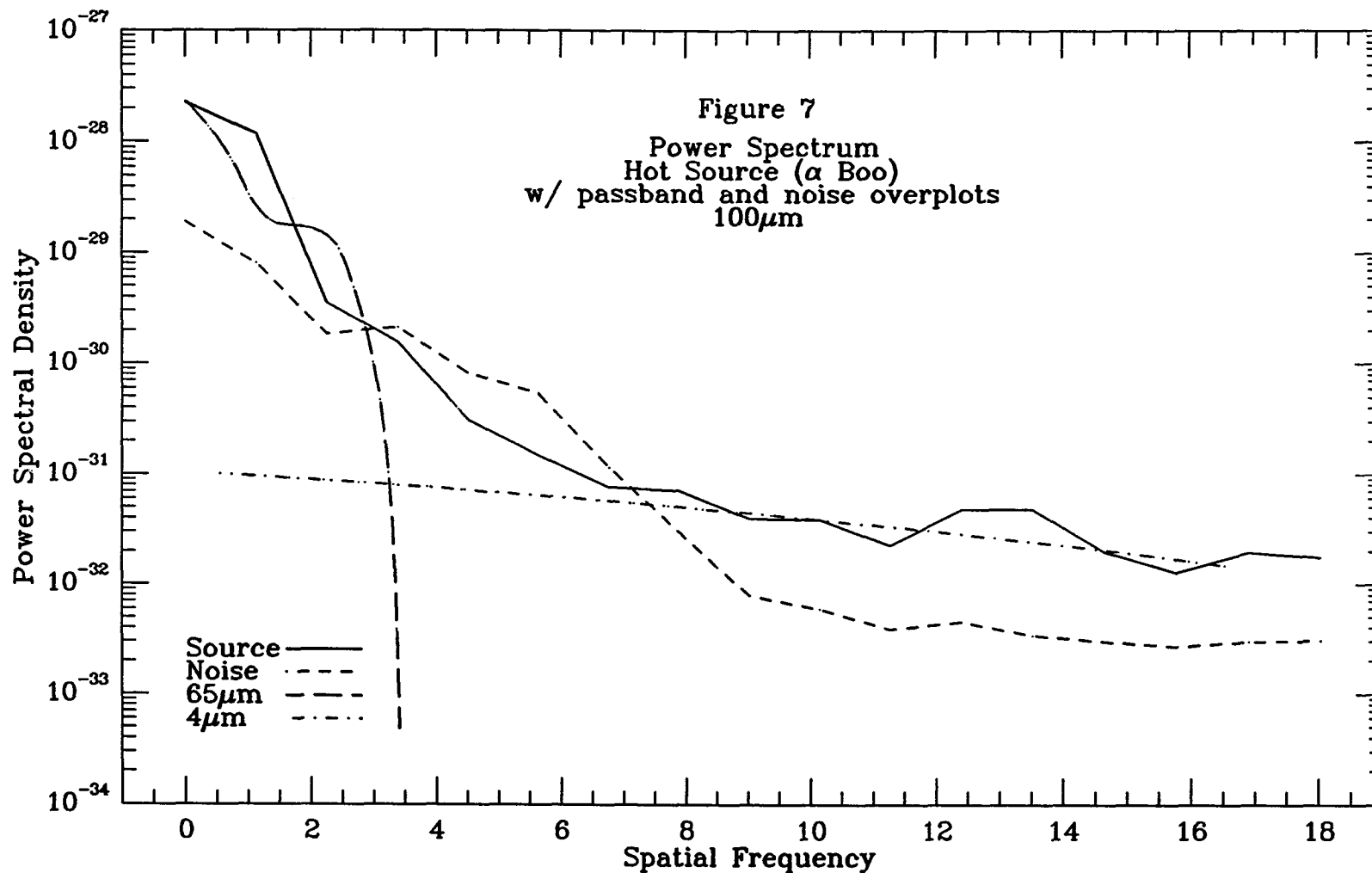


Fig. 7 Power spectrum of α Boo with overplots of a detector 6 noise power spectrum (long-dash curve), a $65\mu\text{m}$ passband (short-dash curve) and a $4\mu\text{m}$ passband curve (dot-dash curve). The $4\mu\text{m}$ curve shows the predicted spectrum of a short wavelength leak of $4\mu\text{m}$.

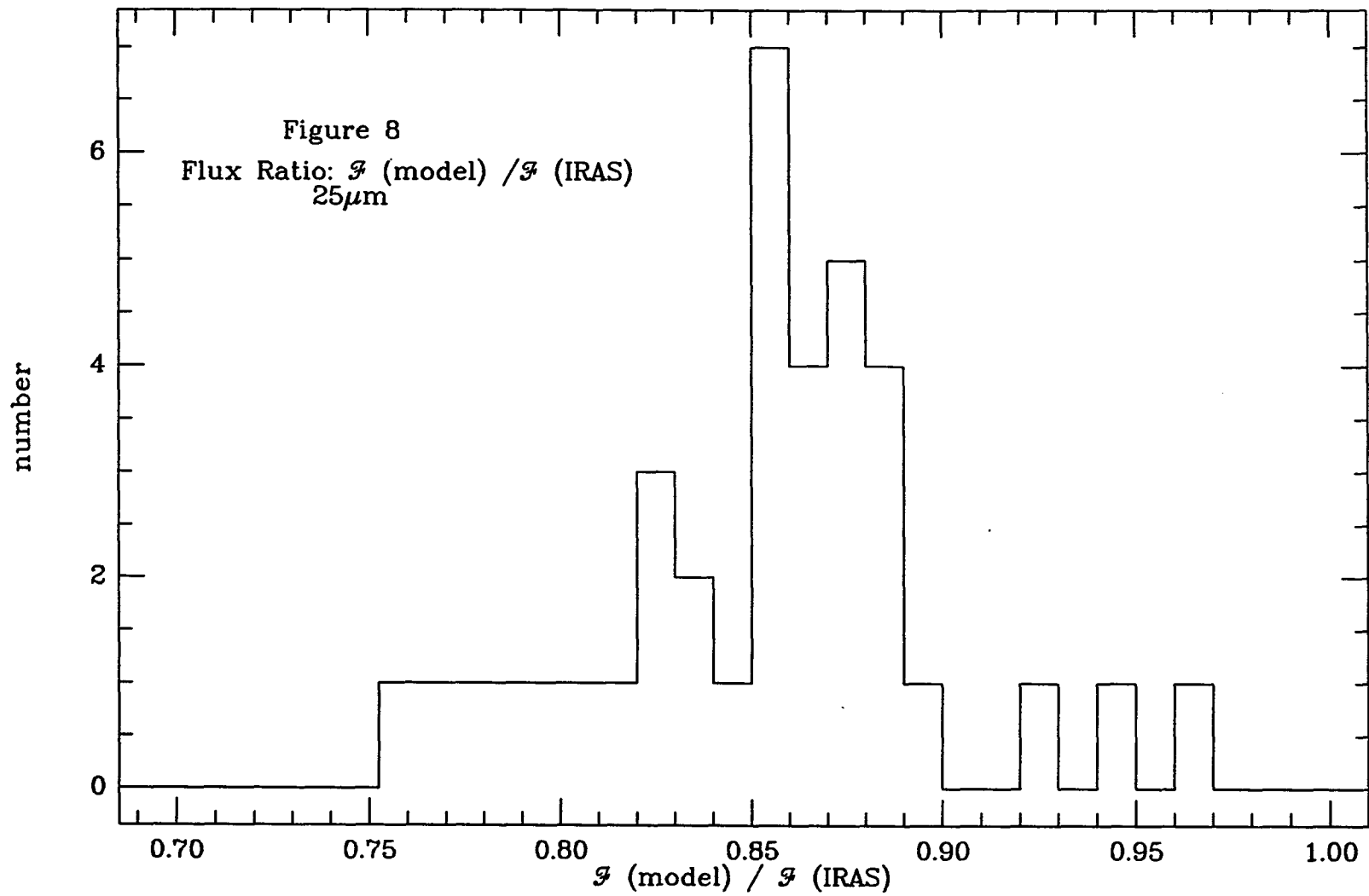


Fig. 8 Shows the dispersion of the ratio of stellar atmosphere predictions to IRAS measurements at $25\mu\text{m}$.

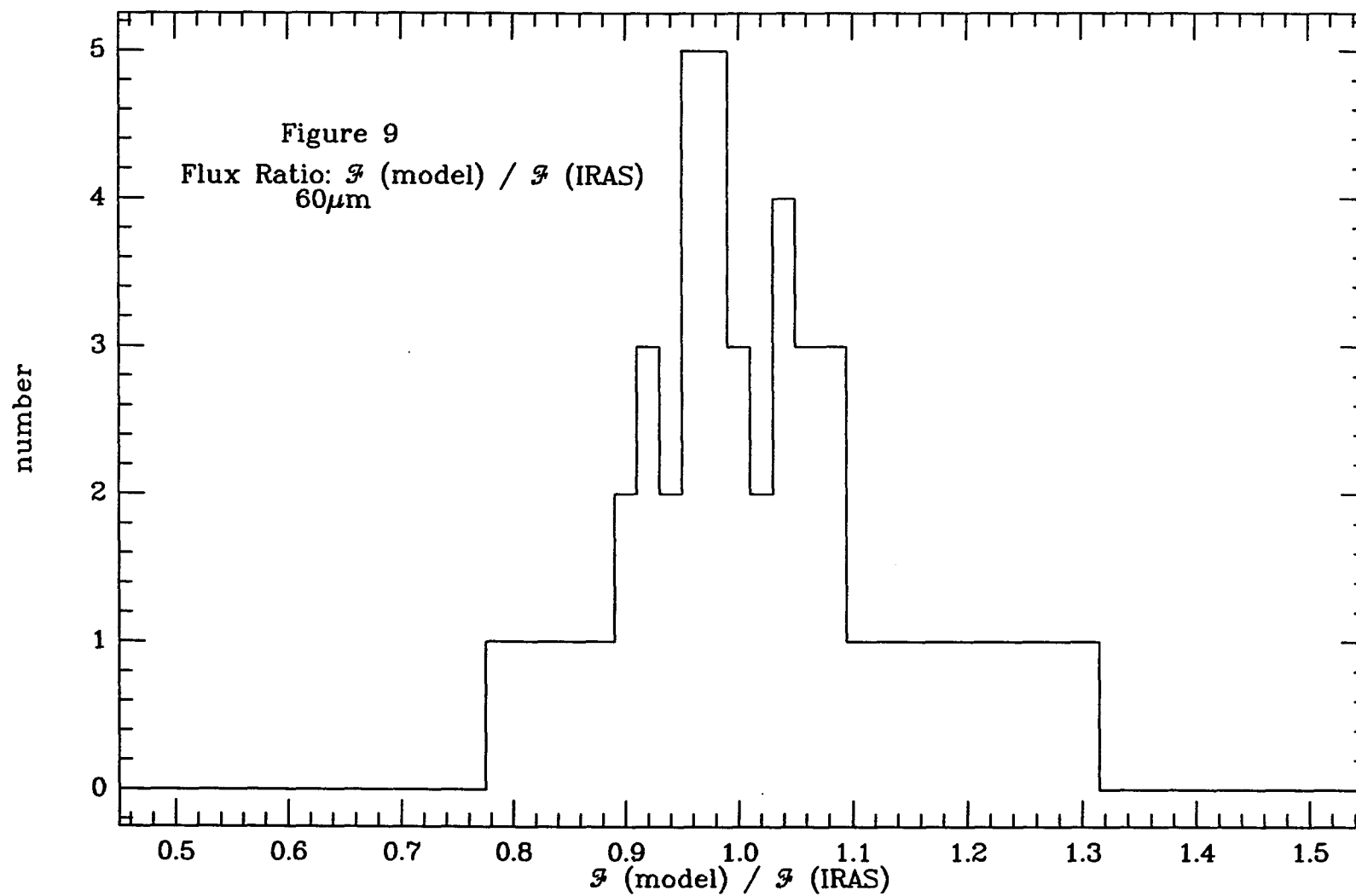


Fig. 9 Shows the dispersion of the ratio of stellar atmosphere predictions to IRAS measurements at 60 μ m.

REFERENCES

- Allen, C.W. (1963). *Astrophysical Quantities*, 2nd ed.
Athlone, London, p.251
- Armstrong, K.R., and Low, F.J. 1974, *Applied Optics*, 13, 425.
- Bracewell, R. (1965). *The Fourier Transform and Its Applications*, New York: McGraw-Hill.
- Campins, C., Rieke, G.H., and Lebofsky, M.J. (1985) *Astron. J.* 90, 896.
- Explanatory Supplement to the IRAS Faint Source Survey, Version 1, ed. M. Moshir, G. Kopan, T. Conrow, H. McCallon, P. Hacking, D. Gregorich, G. Rohrbach, M. Melnyk, W. Rice, L. Fullmer, J. White, and T. Chester. Washington, DC: US Govt. Print. Off., 1989.
- Explanatory Supplement to IRAS Catalogs and Atlases, ed. C.A. Beichman, G. Neugebauer, H.J. Habing, P.E. Clegg, and T.J. Chester. Washington, DC: US Govt Print. Off., 1984
- Gustaffson, B., Bell, R.A., Eriksson, K., Nordlund, A., 1975, *Astron. & Astrophys.*, 42, 407.
- Kurucz, R. L., 1979 *Ap. J. [Suppl]*, 40, 1
- Kurucz, R. L., 1990, Preprint, to be published in *Precision Photometry: Astrophysics of the Galaxy*. Schenectady: L. Davis Press, 1991.
- Kurucz, R. L., 1991, private communication
- Lebofsky, L.A., Sykes, M.V., Nolt, I.G., Radostitz, J.V., Veeder, G.J., Matson, D.L., Ade, P.A.R., Griffin, M.J., and Gear, W.K., 1985, *Icarus*, 63, 192.
- Low, F.J., and Rieke, G.H. (1974) In *Methods of Experimental Physics*, edited by N. Carleton (Academic, New York), Vol 12, p. 456.
- Low, F. J., 1990, private communication
- Press, W. H., Teukolsky, S. A., Flannery, B. P., Vetterling, W. T., 1989, *Numerical Recipes* (New York: Cambridge University Press)

- Rieke, G.H., Lebofsky, M.J., and Low, F.J. (1985) *Astron. J.* 90, 900
- Tokunaga, A.T. 1984. *Astron. J.* 89, 172.
- A User's Guide to IRAS Pointed Observation Products, ed. E.T. Young, G. Neugebauer, E. L. Kopan, R.D. Benson, T.P. Conrow, W. L. Rice, D. T. Gregorich. Greenbelt, Md: National Space Science Center, 1985.
- Vernazza, J. E., Avrett, E. H., and Loeser, R. 1976 *Ap. J. [Suppl]*, 30, 1